Raman metrics for molybdenum disulfide and graphene enable statistical mapping of nanosheet populations

Article (Accepted Version)

Article

Raman metrics for molybdenum disulfide and graphene enable statistical mapping of nanosheet populations

Aline Amorim Graf, Sean P. Ogilvie, Hannah J. Wood, Christopher J. Brown, Manoj Tripathi, Alice A. K. King, Alan B. Dalton, and Matthew J. Large

Chem. Mater., **Just Accepted Manuscript** • DOI: 10.1021/acs.chemmater.0c02109 • Publication Date (Web): 29 Jun 2020

Raman metrics for molybdenum disulfide and graphene enable statistical mapping of nanosheet populations

Aline Amorim Graf[1*], Sean P. Ogilvie[1], Hannah J. Wood[1], Christopher J. Brown[1], Manoj Tripathi[1], Alice A. K. King[1], Alan B. Dalton[1], Matthew J. Large[1*]

[1] University of Sussex, Brighton, BN1 9QH, United Kingdom.

a.amorim-graf@sussex.ac.uk; m.large@sussex.ac.uk

Abstract

The growing research interest and uptake of layered nanomaterials for real-world applications require efficient, reliable, high-quality characterisation methods. Liquid-exfoliated graphene has well-established Raman spectroscopic metrics for mean size and thickness. In association with the mapping process described here, distributions of nanosheet properties can be reconstructed. Here, we develop new, robust metrics for length and layer number of MoS_2 nanosheets, developed using resonant Raman spectroscopy, applicable to both liquid- and mechanically-exfoliated MoS_2. The use of metricised Raman mapping analysis, here demonstrated for graphene and MoS_2, facilitates the standardisation of characterisation, allowing the correlation of size- and thickness-sensitive applications' performance with materials properties.

Introduction

As layered nanomaterials become more widespread there has been growing concern over the quality of the materials supply. In particular, there has been increasing demand for standardisation of methods and metrics to ensure reproducibility of materials and results, as well as appropriate definitions of materials[1–5]. The International Organization for Standardization published a list of vocabulary terms to accelerate the uptake of graphene materials in industry[6]. To date, many efforts to standardise approaches and characterisation have focused on graphene. It

is the most widely-recognised archetypal layered material, and has the greatest prospects for short-term acceptance in applications. However, it is clear that other layered nanomaterials, such as hexagonal boron nitride and transition metal dichalcogenides (TMDs), will eventually suffer the same concerns regarding material quality and reproducibility. TMDs are a class of interesting materials because of their wide range of semiconducting and optoelectronic properties, e.g. photoluminescence[7–9], *n*- or *p*-type behaviour[10,11], and catalytic performance[12,13].

Liquid phase exfoliation (LPE) of layered materials has been shown to achieve high production rates[14,15] and high material quality[16–18], albeit for small lateral particle sizes[19]. Additionally, LPE processes necessarily produce a distribution of particle sizes and thicknesses. Although centrifugation-based size selection can separate particles approximately by layer number[20], robust methods are necessary to characterise the relevant nanosheet properties such as layer number, length and distribution parameters. In particular, the average layer number (and layer number range) are important since accessible surface area is a dominant performance indicator in many applications, such as reinforcement in composites, catalytic activity, and electrochemical energy storage devices, regardless of the specific material properties.

Microscopy-based characterisation provides complete information regarding a sample's layer number and length distributions. Properly representative number-average values may be obtained, but these techniques are usually time-consuming and heavily dependent on good sample preparation[3]. Even though spectroscopy techniques provide volume averages, more representative analysis can be developed in association with microscopic verification[21,22]. Raman spectroscopy is a powerful non-destructive characterisation tool with high-throughput and yet Raman metrics for various layered materials and different exfoliation techniques are underdeveloped. In this paper, we develop both metrics and a methodology for understanding nanosheet size and thickness distributions.

Experimental methods

Liquid-phase exfoliation: Graphite powder (Zenyatta Ventures Ltd.) at initial concentration of 25 mg ml^{-1} (20 mL total volume) was dispersed in cyclohexanone (Sigma Aldrich) and probe sonicated using the Sonics Vibracell VCX-130 and the 1/2 inch (13 mm) tip for 3h at 60% amplitude. The resulting dispersion was centrifuged for 30 min at 5000 *g*. Supernatant was collected for further characterisation. MoS_2

dispersions were prepared using a high-pressure homogenisation process as described by Large *et al.*[23].

Liquid cascade centrifugation: The homogenised MoS_2 dispersion in aqueous surfactant (Triton X-100) was submitted to an initial centrifugation step at 3000 *g* for 5 min to remove any unexfoliated material. The supernatant was used to start the cascade. The dispersion was centrifuged at relative g-force of 3000 *g* for 9 min. The resulting sediment was redispersed in Triton X-100 at a concentration of 0.5 g/L and the procedure was repeated to select narrow size distributions for subsequent 12 min, 14 min, 20 min, 40 min, 1h, 2h, 4h, 8h, and 12h steps to produce the samples. The samples are always referred to using the time of centrifugation, since relative g-force was kept constant.

Mechanical-exfoliation: Mechanically-exfoliated MoS_2 was produced using a variation on the Scotch tape method. A natural bulk MoS_2 crystal (CrystalAge.com) was pressed into contact with 3M Scotch Magic tape and peeled. In a second step, clean tape was pressed into contact with the peeled material and removed to exfoliate the MoS_2 layers; this was repeated up to 6 times, using fresh tape each time. The exfoliated MoS_2 was transferred from the tape to a PDMS slab (QSil 216, Farnell) which was cast against a glass surface and cured at 140°C prior to the transfer. To transfer the exfoliated MoS_2, the cast surface of the PDMS was peeled off of the glass and pressed into contact with the tape, and heated at 120°C on a hotplate under moderate pressure for 2-3 minutes. The tape was removed while heat was applied to maximise transfer of the exfoliated MoS_2, and minimise transfer of tape adhesive residue. The same heating-pressure-lifting step was used to transfer the exfoliated MoS_2 off of the PDMS transfer substrate onto the final target substrate (Si wafer or Si with a 300-nm layer of the thermal oxide SiO_2).

Raman spectroscopy: Samples were prepared by drop casting dispersions onto silicon wafer heated above the boiling point of water to remove any residual solvent in the analysed sample, and to minimise re-aggregation of the nanosheets during drying. As much as possible, the mass per unit area of material deposited for analysis was kept constant. Uniformity of the samples was analysed in the SI.

The spectra are taken using a Renishaw inVia™ confocal Raman microscope. Non-resonant measurements used an excitation laser wavelength of 532 nm whereas the resonant spectra a 660 nm laser. Both measurements used an 1800 mm^{-1} grating. Maps follow the experimental procedure of using the highest magnification available (100x, NA 0.85) unless stated otherwise. A further discussion about the effect of magnification on the maps follows in the SI.

Step size for the maps was chosen according to the objective resolution limitation. The size of the focus spot may be calculated using the following equation:

$$\text{Spot size} = \frac{1.22\ \lambda_{EX}}{\text{NA}}$$

where λ_{EX} is the excitation wavelength and NA is the numerical aperture of the objective. However, for a confocal Raman system, the lateral resolution is defined as the minimum distance between two points for them to be resolved as two different objects. The equation for lateral resolution is[24]:

$$\text{Lateral resolution} = \frac{0.61\, n\, \lambda_{EX}}{\sqrt{1+\beta^2}\,\text{NA}}$$

where n is the refractive index of the medium, and $\beta = \frac{\lambda_{EX}}{\lambda_{DT}}$ is the ratio between the excitation and detection wavelengths. We use the silicon mode at 520 cm^{-1} as the reference, since it is at a higher Raman shift than the MoS_2 Raman modes studied, it corresponds to the lowest resolution, around 300 nm for both lasers.

The area being analysed was set to a minimum of 100 μm^2, in order to achieve high statistical power. Laser power and acquisition time were varied between graphene and resonant and non-resonant MoS_2 maps to reflect the changes in number of counts for the different materials and excitation energy. Laser power and acquisition time were kept constant for every series of maps; of the order of 1 mW and hundreds of milliseconds, respectively.

Maps were baseline corrected and the cosmic rays removed using the WiRE™ software before being analysed using a MATLAB script. For the baseline, the software uses an "intelligent fitting", which automatically excludes regions with peaks and fits the rest of the spectrum using a polynomial approximation. Smoothing was done in two steps, using 3-point median filter first, then a 5-point Gaussian smoothing (further discussion is given in in SI).

Atomic force microscopy: Samples used for Raman spectroscopy mapping were also used for AFM characterisation. The Dimension Icon system from Bruker operating in the Peak Force Tapping mode (Quantitative Nanomechanical property mapping) was used. The probe used was a ScanAsyst Air tip whose spring constant is 0.4 N m^{-1}, and a tip-sample contact force of 5.0 nN was used for all measurements. AFM thicknesses were converted to layer number by following an established methodology[3,25]. Each flake height was measured and plotted with all measurements arranged in ascending order. The first plateau in the data indicates the thickness of the monolayer. The difference between subsequent plateaux positions indicate the interlayer spacing.

UV-vis spectroscopy: UV-vis spectra were measured in quartz cuvettes (Starna Scientific) using the Shimadzu UV-3600 Plus spectrophotometer.

Dynamic light scattering: Particle size was determined using an Anton Paar Litesizer 500 with a 658 nm laser (40 mW).

Results and discussion

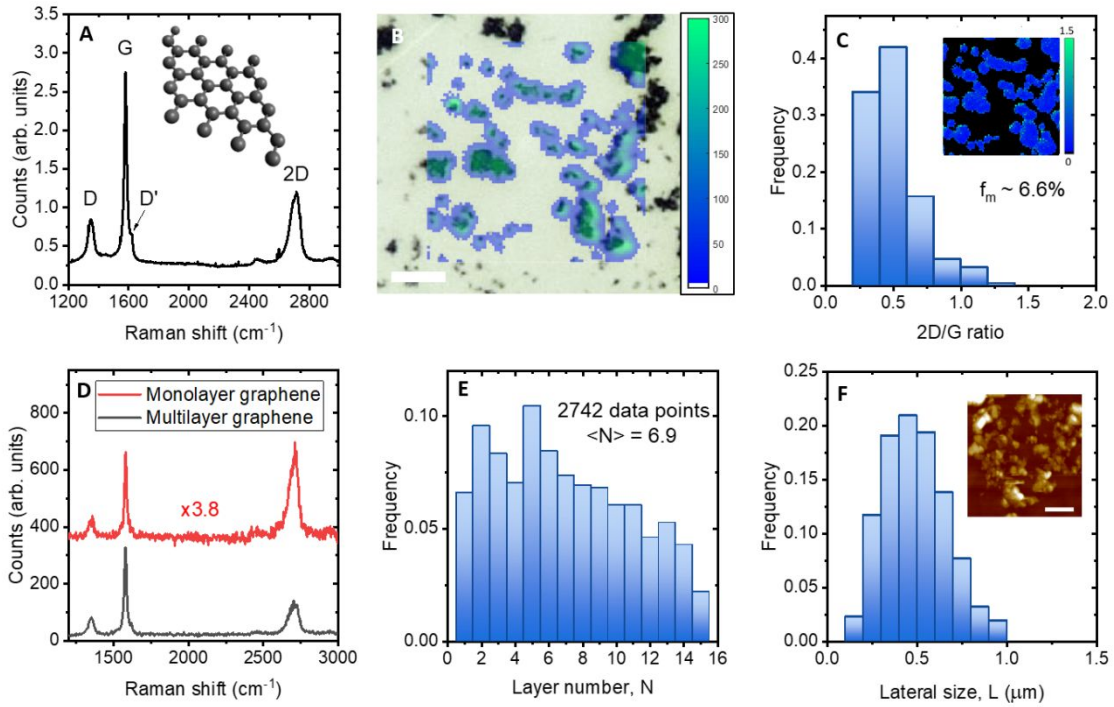

*Figure 1: **A**: Raman spectrum averaged over a large area of a LPE graphene film prepared by hotplate deposition. Graphene Raman modes are labelled. **B**: Optical micrograph and associated Raman map of G-peak intensity over a 20x20 μm area of the sample. The scale bar is 5 μm. **C**: Histogram of the 2D/G peak intensity ratio (evaluated pixel-wise from the inset 2D/G ratio map). **D**: Individual pixel spectra for a larger multilayer nanosheet and a monolayer nanosheet. The monolayer spectrum has been normalised relative to the 2D peak, and offset, for clarity. **E**: Metric-derived layer number distribution from the data in **C**. **F**: Metric-derived nanosheet lateral size distribution based on analogous analysis of the D/G peak intensity ratio. (inset) AFM of a 1x1 μm area of the same sample. The scale bar is 500 nm.*

Graphene has well-established metrics for mean layer number and lateral size for LPE nanosheets. **Figure 1A** shows a typical Raman spectrum of LPE graphene. The main modes of interest are the G (C-C bonding), D (a defect-activated mode indicating presence of grain boundaries, edges, or basal plane defects), and 2D peaks (an overtone of the D peak containing information on inter-layer coupling)[26–28]. In order to demonstrate how Raman can be used to achieve a more thorough analysis of particle size distributions we adopt the Raman metrics of Backes *et al.*[29], which relate the average layer number of a graphene nanosheet sample $\langle N \rangle$ to the intensity ratio of the 2D and G peaks:

$$\langle N \rangle = 1.04 \left(\frac{I_{2D}}{I_G} \right)^{-2.32}, \quad (1)$$

as well as the average lateral size $\langle L \rangle$ to the ratio of D- and G-peaks:

$$\langle L \rangle = \frac{0.094}{(I_D/I_G)_{graphene} - (I_D/I_G)_{graphite}} \quad (2)$$

where $(I_D/I_G)_{graphite}$ is the D/G intensity ratio for the unexfoliated graphite.

Our measurement process is to map the Raman spectra of a sample area using high magnification (x100 objective, NA 0.85) and pixel size determined by the calculated lateral resolution limit of the objective. Further discussion about the map parameters, the magnification effect on the maps and the peak threshold can be found in the SI. The samples are prepared with a low areal density to minimise aggregation, by drop casting on a hotplate (set 10°C to 20°C above the dispersion boiling point). This approach to achieving higher statistical power from a Raman measurement is not unusual, however rather than sum all pixel spectra we process them individually using the metrics above. This produces a set of maps representing pixel-wise analysis of layer number and lateral size, from which histograms are plotted. Importantly, this method reconstructs particle size *distributions* that are close to the population distribution rather than simply measuring averages. **Figure 1B** shows an optical micrograph of a typical LPE graphene sample with an overlaid Raman map (showing the G peak intensity). This 20 by 20 μm area contains 6561 spectra, which have been thresholded based on their G peak intensity using a MATLAB script to eliminate 'empty' pixels. The resulting sample contains 2440 Raman spectra.

Figure 1C shows a histogram of 2D/G peak ratio derived from the data illustrated in **Figure 1B**. Inset is a map of the 2D/G ratio, showing that higher values (which are related to lower layer numbers, with a ratio >1 indicating a monolayer particle) are concentrated at the edges of larger aggregates of particles. In order to understand this phenomenon, individual pixel spectra are investigated in **Figure 1D**. The two spectra shown are one with a 2D/G value greater than 1 (indicative of a monolayer) and one with a value close to the average of the distribution in **Figure 1C**. When a monolayer and a multilayer particle are both present in the focal spot, the 'summed' spectrum representing both particles is heavily skewed towards the multilayer, based on the larger particle volume and optical absorption of the multilayer. This effect means that a low-magnification spectrum of a given sample, with a broad layer number distribution, will over-represent thicker multilayers and under-represent

any few-layer content; an effect that is mitigated by mapping analysis. Comparison of the spectrum in **Figure 1A** with the multilayer spectrum in **Figure 1D** illustrates this volume-weighting effect.

Once we apply appropriate metrics to the data in a pixel-wise fashion, binning the resulting layer numbers and lateral sizes produces distributions representing the population of nanoparticles. These are shown in **Figure 1E** and **F**, and are distributions by particle area rather than number or volume, due to the measurement approach. The inset of **Figure 1F** shows AFM data of the film, where the scale bar is equal to the average lateral size estimated from the Raman-derived distribution (360 nm). **Figure S5** compares the Raman-derived layer number distribution to the AFM pixel height distribution, which suggests that the apparent interlayer spacing is in the range 0.7 to 0.8 nm; agreeing strongly with previous measurements for LPE graphene[15,16]. The average of the layer number distribution in **Figure 1E** is $\langle N \rangle = 4.7$, however when we apply the metric to the averaged spectrum for the whole map (shown in **Figure 1A**) we arrive at $\langle N \rangle = 8.7$. This large over-estimation reflects the idea that, in samples with broad distributions of layer number, the thicker multilayers contribute more significantly to the overall sample signal, thereby skewing results towards greater $\langle N \rangle$. Evidently, applying our mapping approach it is possible to both improve reliability of average property measurements as well as to reconstruct approximate size and thickness distributions. Reconstruction of population distributions would require one nanosheet per pixel. Our method obtains the greatest amount of information possible when practical considerations are made, particularly the time required to achieve high enough statistical power and the challenges of producing sparse enough samples for high-quality measurements to be obtained.

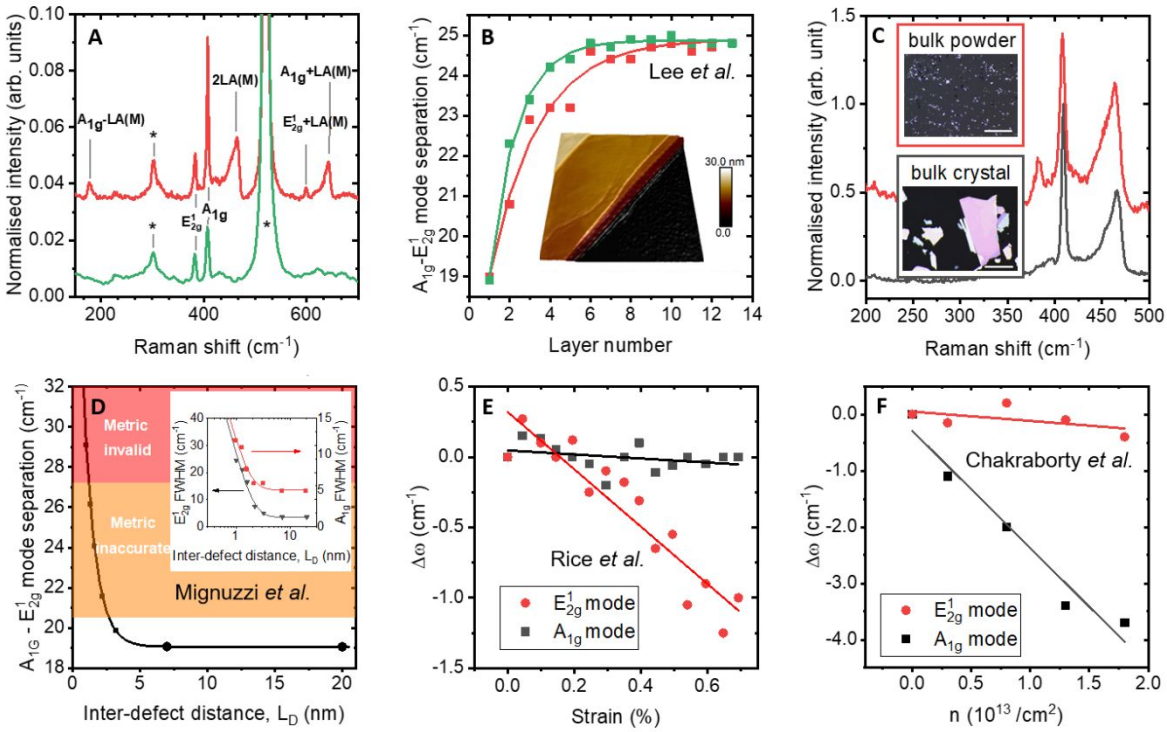

Figure 2: ***A:*** *Raman spectra of a film of MoS_2 prepared by deposition of a LPE dispersion. Both resonant (red curve) and non-resonant (green) conditions are shown. Peaks were labelled with the associated symmetry group[30,31]. A table containing the corresponding Raman shifts is in SI. The peaks attributed to the silicon substrate are indicated with an asterisk (*).* ***B:*** *Modification of the A_{1g} and E^1_{2g} modes separation with varying layer number for mechanically-exfoliated MoS_2 (data from Lee* et al. *[32]). Fitted curves are of the form $\Delta\nu = \Delta\nu_{bulk} - Ae^{-N/b}$. Inset includes a 3D plot of an AFM micrograph showing different plateaux corresponding to different layers in a mechanically-exfoliated sample.* ***C:*** *Raman spectra of bulk MoS_2: for a crystal used for ME (black) and powder used for LPE (in red). Optical micrographs show the corresponding material at the same magnification. Scale bar is 20 µm.* ***D:*** *Measure modification to the mode separation in monolayer MoS_2, as a function of inter-defect distance L_D, based on spectra from Mignuzzi* et al.[33]. Highlighted areas show where the mode separation metric showed in **B** becomes inaccurate and invalid. Inset shows the measurements of the full width at half maximum (FWHM) for the A_{1g} *and* E^1_{2g} *Raman modes with L_D based on the same data.* ***E-F:*** *The same mode separation is plotted as a function of applied uniaxial strain (replotted data from Rice* et al.[34]) and *doping (replotted data from Chakraborty* et al.[35]).

The same mapping methodology can be applied to MoS_2, the well-studied archetypal TMD[25,30,36]. MoS_2 is a layered semiconducting nanomaterial, with an indirect bandgap of 1.2 eV in the bulk that shifts to a direct gap of 1.95 eV in the monolayer[37]. Non-resonant Raman spectroscopy reveals two main vibrational modes: E^1_{2g}, corresponding to in-plane lattice vibrations and A_{1g}, the out-of-plane vibrations (notation used is according to representations of the D_{6H} group used for bulk-like MoS_2[38]). Additional information can be gained through the use of resonant Raman spectroscopy, where resonance of the excitation with an electronic transition amplifies

signal intensity and relaxes the selection rules for Raman scattering, allowing multi-phonon processes[39]. Second-order Raman scattering processes are enhanced by the coupling of phonon modes to optically-excited electronic states[40]. In the case of MoS_2, the presence of an exciton absorption near 670 nm[25] (1.86 eV, very weakly dependent on layer number) facilitates resonant excitation using a 660 nm (1.88 eV) laser. Resonant (660 nm excitation) and non-resonant (532 nm, or 2.33 eV, excitation) spectra of a film prepared from an LPE dispersion are shown in **Figure 2A**. A table of Raman shifts and mode assignments is in the SI. For the non-resonant spectrum, the two expected modes are visible in addition to modes associated with the silicon substrate. The resonant spectrum is more complex; in addition to the main modes, an intense peak assigned to the second-order longitudinal acoustic mode at the M point, 2LA(M) (around 460 cm^{-1}), is observed. Other additional vibrations at higher Raman shift are associated with combination modes involving the LA(M) mode[37].

It is known that the E^1_{2g} mode softens for increasing number of layers while the A_{1g} mode stiffens, although only in the few-layer limit ($N < \sim 10$). The resulting increase in peak separation between the main modes with increasing number of layers may be used for characterising MoS_2 nanosheets. **Figure 2B** shows data for mechanically-exfoliated (ME) nanosheets from Lee *et al.*[32] for two different excitation energies. The peak separation saturates quickly hindering the distinction between number of layers bigger than six. The constants of the fitted functions are laser dependent but the form is the same for both cases: $\Delta\nu = \Delta\nu_{bulk} - Ae^{-N/b}$. Since the fitting relies on characterising the bulk form, **Figure 2C** shows Raman spectra of bulk powder (red) used for our LPE experiments and a bulk crystal (black) used for ME. The insets are optical micrographs under the same magnification highlighting the differences in morphology. It is noted that the spectra are non-identical even though they are both "bulk" forms of MoS_2. The main difference is that the intensity of the E^1_{2g} mode for the crystal approaches the spectrum baseline.

Another influence affecting the main mode positions is the defect density. A plot of A_{1g} and E^1_{2g} mode separation for varying inter-defect distance is shown in **Figure 2D;** data replotted from Mignuzzi *et al.*[33]. **Figures 2E** and **2F** illustrate the shifts observed as a function of applied uniaxial strain (data replotted from Rice *et al.*[34]) and doping (data replotted from Chakraborty *et al.*[35]), respectively. Even though the metric using the A_{1g} and E^1_{2g} mode separation is useful, some effects that cause shifts to the

peak positions are often neglected, and can significantly complicate the interpretation of measurements, as **Figure 2** demonstrates.

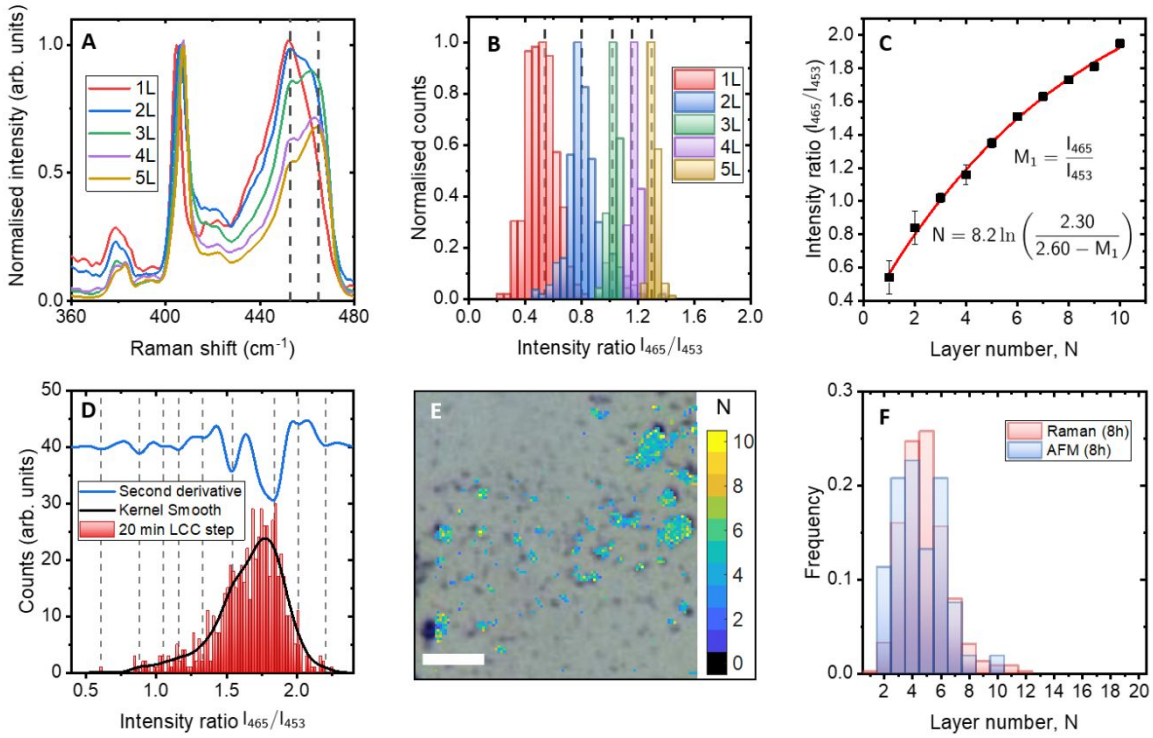

Figure 3: ***A:*** *Normalised Raman spectra for ME nanosheets of varying layer number. Dashed lines indicate the positions of Raman features at 453 and 465 cm^{-1}.* ***B:*** *Histograms of the intensity ratio I_{465}/I_{453} plotted from different maps of ME samples with varying number of layers.* ***C:*** *Graph of layer number against the centre of the histograms in B. The fitted function is of the same form as peak separation metric, with the inverted equation shown.* ***D:*** *Histogram of the I_{465}/I_{453} ratio for an LCC step of LPE nanosheets with a broad distribution of layer number. Second derivative curve (blue) of smoothed histogram (black) is shown. Dashed lines indicate peak positions, in agreement with data for ME sheets (see SI).* ***E:*** *Optical micrograph overlaid with corresponding Raman map of a 20 µm by 20 µm area of a LPE sample. Raman map is colour coded according to the layer number metric in D. Scale bar is 5 µm.* ***F:*** *Plots of layer number distribution from AFM (red) and the present Raman metric (blue) for the same LPE sample shown in panel E.*

In order to investigate alternative metric approaches, we studied ME MoS_2. This process is known for producing large and well-exfoliated nanosheets. By investigating this system initially, edge and length effects on the Raman spectra are dismissed and the primary influence comes from the layer number. **Figure 3A** shows resonant spectra normalised to the A_{1g} mode for different numbers of layers. The main variation is associated with the 2LA(M) feature, which is actually comprised of two different modes: one centred at 453 cm^{-1} and the other at 465 cm^{-1}, respectively, where their relative intensity appears to be determined by the layer number. The first peak is usually associated with the 2LA(M) mode and the second one does not have a

formally-agreed assignment in the literature. It might be associated with an infrared active mode (A_{2u})[37,41] or a mode involving an acoustic vibration[40,42]. It is interesting to note that the relative intensities of these modes is fully independent of laser focus, as seen in the SI.

Histograms of the intensity ratio I_{465}/I_{453} for maps of several ME nanosheets are shown in **Figure 3B**. The histograms are narrow with non-overlapping centres. Plotting the central I_{465}/I_{453} ratio against the layer number for each sample allows us to fit a metric equation of the same form as the A_{1g} and E^1_{2g} mode separation ($\Delta\nu = \Delta\nu_{bulk} - A\, e^{-N/b}$) but with the advantage of avoiding effects that influence peak positions by using an intensity ratio; this is shown in **Figure 3C**. Having measured the ratio I_{465}/I_{453}, the following equation returns the layer number:

$$N = 8.2 \ln\left(\frac{2.3}{2.6 - \frac{I_{465}}{I_{453}}}\right) \quad (3)$$

This equation was developed using a mapping analysis and it can reconstruct the approximate distribution this way, however it can determine layer number accurately for single-point spectra as well. The fitting parameters and respective uncertainties are: $(8.2 \pm 1.1); (2.30 \pm 0.13); (2.60 \pm 0.16)$. Histograms of the I_{465}/I_{453} ratio were plotted for every sample in a liquid cascade centrifugation (LCC) experiment using LPE MoS_2 and the mapping methodology described in **Figure 1**. LCC selects different fractions from the broad distribution of sizes and thicknesses produced by LPE using sequential centrifugation steps (from 9 min to 12 h, at 3000 *g*)[43]. The histograms were smoothed using a weighted average of adjacent points (kernel smooth technique). The second derivative of the resulting curve indicates, from the local minima, the position of underlying peaks in the data, even if they are not resolved. **Figure 3D** shows the raw histogram, kernel-smoothed curve, and second derivative for one LPE sample with a broad distribution of I_{465}/I_{453} ratios. A table with the peak positions identified in the histogram analysis is in SI. There is exceptional agreement between the ratios for both LPE and ME techniques (see SI). This fact highlights that even though the exfoliation processes are different the same variation in the Raman spectra is observed with layer number. Also, it indicates the robustness of our metric in comparison to the literature approach because ME sheets will have varying degrees and orientation of strain, which should be different for solution-processed nanosheets

(see SI). This allows the I_{465}/I_{453} intensity ratio to be used as a metric to analyse layer number distributions for both LPE and ME nanosheets. The fitting constant multiplying the independent variable in the exponential form $y = y_0 - Ae^{-(x-x_0)/b}$ indicates the applicable range for our metric. This constant is 8.2 for our fitting, allowing measurement up to ~16 layers before the exponential scaling makes layer numbers indistinguishable. The same constant for the literature metrics presented in **Figure 2B** is 2.2, so that limit is closer to 5.

Figure 3E shows an optical micrograph and overlaid Raman map colour coded according to the number of layers. The Raman layer number distribution is compared with AFM measurements for the same sample in **Figure 3F**. There is a good agreement between the two techniques. Identical analysis is shown in the SI **(Figure S9)** for every step of an LCC experiment.

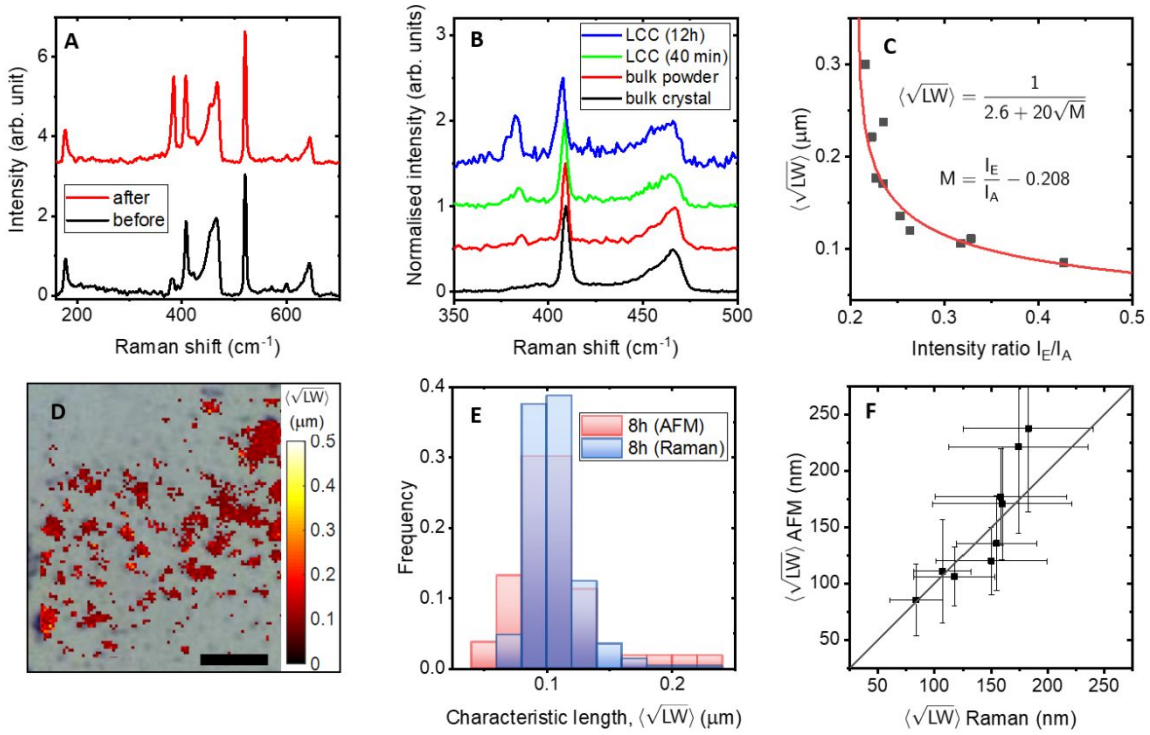

Figure 4: ***A:*** *Raman spectra before (black) and after (red) inducing defects on a ME nanosheets with a laser. The relative increase in intensity of the E^1_{2g} mode is correlated with an increasing number of defects.* ***B:*** *Raman spectra of samples with different sizes are shown. The smallest length shown here is represented by the blue curve, followed by the green one. They are both steps in a LCC. LPE bulk powder is in red and ME bulk, black. Decreasing nanosheet size shows increase in relative intensity of the E^1_{2g} mode.* ***C:*** *Plot of the main modes intensity ratio (I_E/I_A) against the inverse of the characteristic length.* ***D:*** *Optical micrograph overlaid with corresponding Raman map of a 20 μm by 20 μm area of a LPE sample. Scale bar is 5 μm.* ***E:***

Histogram of length distribution from AFM (red) and Raman metrics (blue) for the same sample in D. ***F:*** *Plot of nanosheets length measured from AFM micrographs and Raman maps showing good correlation between the techniques.*

A length metric for MoS_2 may be developed based on an analogous analysis to that employed for graphene[29]. For graphene, the intensity ratio of the G and D modes is used. The G mode written as an irreducible representation is of the form E_{2g}, which may be compared to the E^1_{2g} mode in TMDs since they both involve in-plane vibrations[38]. The D band in graphene is a disorder-induced vibration and a similar feature in TMDs is the LA(M) mode, around 225 cm^{-1}. However, this vibration is absent in our measurements of pristine MoS_2. This mode is observed in the literature when there are defects with dangling bonds[44]. In order to find an alternative defect-enhanced mode, a study based on laser damage was performed on ME nanosheets and the results shown in **Figure 4A**. Spectra were taken before and after the laser was left on for ten seconds at high power. There is a significant change in the relative intensity of the A_{1g} and E^1_{2g} modes, with the E^1_{2g} intensity increasing significantly, as the laser induces basal plane damage. We do not observe the same increase in E^1_{2g} intensity at the edges of our ME sheets, however the same increase *was* observed for an electrochemical oxidation experiment on ME sheets, discussed in the SI. These observations potentially allude to differences in spectral behaviour with defect type.

Figure 4B illustrates the A_{1g} and E^1_{2g} mode intensity variation for different nanosheet lengths. The average length according to AFM measurements is 85 nm for the smallest fraction in the LCC series, and 171 nm for an intermediate step. Bulk powder used for the LPE experiment is ~340 nm, while the bulk crystal used for ME is at least two orders of magnitude larger. The intensity of the E^1_{2g} mode increases monotonically with decreasing nanosheet length, corroborating measurements by Huang *et al.*[44] at the edges and basal planes of mono and bilayer MoS_2. Considering the nanosheet edges to have a higher defect density than the basal plane, it is clear that defect-related modes would be more prominent for smaller sheets, where the ratio of perimeter to basal plane area is greater[29]. This enhancement of the in-plane vibration therefore, in principle, should allow the use of the A_{1g} and E^1_{2g} mode intensities as an analogous sheet length metric to that for graphene.

We use a characteristic length in calculations defined as $\langle\sqrt{LW}\rangle$, where *L* is the nanosheet length and *W* is the width. Both dimensions are correlated through an average lateral aspect ratio[20]; further discussion about these quantities is in the SI. A

plot of the relative intensity ratio between the main modes (I_E/I_A) against the characteristic length is shown in **Figure 4C**. The fitted equation is:

$$\langle\sqrt{\mathrm{LW}}\rangle = \frac{1}{2.6 + 20.0\sqrt{\frac{\mathrm{I_E}}{\mathrm{I_A}} - 0.208}} \quad (4)$$

In a similar manner to the layer number metric described, this length metric can be used to reconstruct approximate size distributions in association with the mapping analysis described earlier, and estimates using single-point spectra can be made. The fitting parameters and respective uncertainties are: $(2.6 \pm 1.3)\ \mu\mathrm{m}^{-1}$;$(20.0 \pm 4.0)\ \mu\mathrm{m}^{-1}$;$(0.208 \pm 0.011)$. This metric cannot measure any nanosheets with characteristic length larger than approximately 385 nm (intensity ratio of 0.208), which is equivalent to the bulk powder used for exfoliation (inset of **Figure 3C** and SI). The value inside the square root terms contains a fitted parameter, which represents the limit value of I_E/I_A as $L \to \infty$; that is, we can interpret this value as a measure of the basal plane defect density of MoS_2. We utilise the Spatial Confinement Theory discussed by Kitajima[45] assuming that confined regions with diameter d obey the scaling $I_E/I_A = (c/d)^2$, as is suggested for other MoS_2 mode ratios by Mignuzzi et al.[46]. By assuming that the defects are uniformly distributed we can show that the limit value of I_E/I_A for the fitted equation is related to the basal plane defect density ρ_b by (derivation in SI):

$$\rho_b = \left.\frac{I_E}{I_A}\right|_{1/L=0} \frac{1}{\pi c^2}. \quad (5)$$

Taking an order-of-magnitude estimate for $c = 1\ \mathrm{nm}$ (based on values for graphite[45] and MoS_2[46]) we estimate that our LPE and ME MoS_2 have $\rho_b \approx 7 \times 10^{12}\ \mathrm{cm}^{-2}$ and $5 \times 10^{12}\ \mathrm{cm}^{-2}$, respectively. For comparison, direct measurement by scanning tunnelling microscopy yields a value of up to $10^{13}\ \mathrm{cm}^{-2}$ for ME MoS_2[47].

A Raman map (20 by 20 μm) of a deposited film of LPE MoS_2 is shown in **Figure 4D** with a corresponding optical micrograph. The colour scale indicates the characteristic length determined using equation (4). **Figure 4E** shows the length distributions measured by AFM and Raman of the same sample. Identical analysis is shown in the SI for all steps of the LCC experiment. A correlation plot of the averages measured by both techniques for the different fractions is shown in **Figure 4F**, where the error bars are the standard deviations of the measured distributions. These data

indicate strong agreement between the two techniques; further data showing the agreement of these metrics with other measurement techniques are plotted in the SI. We expect that the choice of surfactant used for the LPE dispersions could cause some degree of doping to the nanosheets, however this effect is anticipated to be minimal. However, the effect of strain and doping on the two components of the 2LA(M) mode is still unknown. We expect that by using an intensity ratio in our calculations, such effects do not hinder a correct layer number and length characterisation.

We have demonstrated a methodology for reconstructing approximate particle size distributions for liquid-exfoliated nanomaterials using Raman microscopy. Graphene and MoS_2 are demonstrated as archetypal materials. We have developed spectroscopic metrics for the layer number and length of MoS_2 nanosheets, which to this point have been absent in the literature. We anticipate that our approach to the development of these metrics can be extended to the other TMDs by virtue of their analogous crystal structures.

Conclusions

Raman mapping performed using the highest available magnification with pixel size determined by the objective lens' lateral resolution reconstructs nanosheet size distributions, as demonstrated for both graphene and MoS_2. A new metric for MoS_2 layer number was developed based on an intensity ratio (I_{465}/I_{453}) of resonant Raman modes, avoiding any mischaracterisation caused by mode shifts resulting from external physical effects such as strain and doping. This metric can be applied to both LPE and ME nanosheets since the correlation between the intensity ratio and layer number is the same in both cases. A metric for LPE nanosheet length using the resonant laser was developed based on the intensity ratio between the two main Raman modes of MoS_2. The Raman mapping analysis combined with both metrics allows a quick and reliable characterisation of size and thickness distributions, paving the way for standardisation of novel nanomaterials and their diverse applications at different scales.

Acknowledgements

The authors gratefully acknowledge A. Henderson for development of the renishawWire.m MATLAB script. We thank Advanced Material Development Ltd for

collaboration on materials production. The authors would like to thank the reviewers for their thorough appraisals, by which the manuscript has been decidedly improved.

Supporting Information Available: Uniformity of samples, magnification study, comparison of distributions for graphene, peak threshold for graphene maps, table of mode assignments for each Raman shift associated with a peak, focal depth dependence of the ratio position of 2LA(M) band maximum, I_{465}/I_{453} and second derivative analysis, correlation between Raman and AFM for average layer number, electrochemical oxidation of ME sheets, characteristic length, I_E/I_A of bulk powder, application of Spatial Confinement Theory, size and thickness analysis for every LCC step, and scaling. This material is available free of charge *via* the Internet at http://pubs.acs.org.

References

(1) Bøggild, P. The War on Fake Graphene. *Nature* **2018**, *562* (7728), 502–503. https://doi.org/10.1038/d41586-018-06939-4.

(2) Kauling, A. P.; Seefeldt, A. T.; Pisoni, D. P.; Pradeep, R. C.; Bentini, R.; Oliveira, R. V. B.; Novoselov, K. S.; Castro Neto, A. H. The Worldwide Graphene Flake Production. *Adv. Mater.* **2018**, *30* (44), 1803784. https://doi.org/10.1002/adma.201803784.

(3) Backes, C.; Higgins, T. M.; Kelly, A.; Boland, C.; Harvey, A.; Hanlon, D.; Coleman, J. N. Guidelines for Exfoliation, Characterization and Processing of Layered Materials Produced by Liquid Exfoliation. *Chem. Mater.* **2017**, *29* (1), 243–255. https://doi.org/10.1021/acs.chemmater.6b03335.

(4) Wick, P.; Louw-Gaume, A. E.; Kucki, M.; Krug, H. F.; Kostarelos, K.; Fadeel, B.; Dawson, K. A.; Salvati, A.; Vázquez, E.; Ballerini, L.; Tretiach, M.; Benfenati, F.; Flahaut, E.; Gauthier, L.; Prato, M.; Bianco, A. Classification Framework for Graphene-Based Materials. *Angew. Chem. Int. Ed.* **2014**, *53* (30), 7714–7718. https://doi.org/10.1002/anie.201403335.

(5) Pollard, A. J.; Paton, K. R.; Clifford, C. A.; Legge, E. *NPL Good Practice Guide 145*; National Physical Laboratory: Teddington, 2007.

(6) Technical committee ISO/TC 229. *ISO/TS 80004-13:2017, Nanotechnologies - Vocabulary - Part 13: Graphene and Related Two Dimensional (2D) Materials*; International Organization for Standardization: Geneva, 2017.

(7) Splendiani, A.; Sun, L.; Zhang, Y.; Li, T.; Kim, J.; Chim, C.-Y.; Galli, G.; Wang, F. Emerging Photoluminescence in Monolayer MoS_2. *Nano Lett.* **2010**, *10* (4), 1271–1275. https://doi.org/10.1021/nl903868w.

(8) Gutiérrez, H. R.; Perea-López, N.; Elías, A. L.; Berkdemir, A.; Wang, B.; Lv, R.; López-Urías, F.; Crespi, V. H.; Terrones, H.; Terrones, M. Extraordinary Room-Temperature Photoluminescence in Triangular WS_2 Monolayers. *Nano Lett.* **2013**, *13* (8), 3447–3454. https://doi.org/10.1021/nl3026357.

(9) Ruppert, C.; Aslan, O. B.; Heinz, T. F. Optical Properties and Band Gap of Single- and Few-Layer $MoTe_2$ Crystals. *Nano Lett.* **2014**, *14* (11), 6231–6236. https://doi.org/10.1021/nl502557g.

(10) Komsa, H.-P.; Kotakoski, J.; Kurasch, S.; Lehtinen, O.; Kaiser, U.; Krasheninnikov, A. V. Two-Dimensional Transition Metal Dichalcogenides under Electron Irradiation:

Defect Production and Doping. *Phys. Rev. Lett.* **2012**, *109* (3). https://doi.org/10.1103/PhysRevLett.109.035503.

(11) Onofrio, N.; Guzman, D.; Strachan, A. Novel Doping Alternatives for Single-Layer Transition Metal Dichalcogenides. *J. Appl. Phys.* **2017**, *122* (18), 185102. https://doi.org/10.1063/1.4994997.

(12) Shi, W.; Fan, K.; Wang, Z. Catalytic Activity for the Hydrogen Evolution Reaction of Edges in Janus Monolayer MoXY (X/Y = S, Se, and Te). *Phys. Chem. Chem. Phys.* **2018**, *20* (46), 29423–29429. https://doi.org/10.1039/C8CP03354D.

(13) Jaramillo, T. F.; Jorgensen, K. P.; Bonde, J.; Nielsen, J. H.; Horch, S.; Chorkendorff, I. Identification of Active Edge Sites for Electrochemical H2 Evolution from MoS2 Nanocatalysts. *Science* **2007**, *317* (5834), 100–102. https://doi.org/10.1126/science.1141483.

(14) Hernandez, Y.; Nicolosi, V.; Lotya, M.; Blighe, F. M.; Sun, Z.; De, S.; McGovern, I. T.; Holland, B.; Byrne, M.; Gun'Ko, Y. K.; Boland, J. J.; Niraj, P.; Duesberg, G.; Krishnamurthy, S.; Goodhue, R.; Hutchison, J.; Scardaci, V.; Ferrari, A. C.; Coleman, J. N. High-Yield Production of Graphene by Liquid-Phase Exfoliation of Graphite. *Nat. Nanotechnol.* **2008**, *3* (9), 563–568. https://doi.org/10.1038/nnano.2008.215.

(15) Paton, K. R.; Varrla, E.; Backes, C.; Smith, R. J.; Khan, U.; O'Neill, A.; Boland, C.; Lotya, M.; Istrate, O. M.; King, P.; Higgins, T.; Barwich, S.; May, P.; Puczkarski, P.; Ahmed, I.; Moebius, M.; Pettersson, H.; Long, E.; Coelho, J.; O'Brien, S. E.; McGuire, E. K.; Sanchez, B. M.; Duesberg, G. S.; McEvoy, N.; Pennycook, T. J.; Downing, C.; Crossley, A.; Nicolosi, V.; Coleman, J. N. Scalable Production of Large Quantities of Defect-Free Few-Layer Graphene by Shear Exfoliation in Liquids. *Nat. Mater.* **2014**, *13* (6), 624–630. https://doi.org/10.1038/nmat3944.

(16) Lotya, M.; Hernandez, Y.; King, P. J.; Smith, R. J.; Nicolosi, V.; Karlsson, L. S.; Blighe, F. M.; De, S.; Wang, Z.; McGovern, I. T.; Duesberg, G. S.; Coleman, J. N. Liquid Phase Production of Graphene by Exfoliation of Graphite in Surfactant/Water Solutions. *J. Am. Chem. Soc.* **2009**, *131* (10), 3611–3620. https://doi.org/10.1021/ja807449u.

(17) O'Neill, A.; Khan, U.; Coleman, J. N. Preparation of High Concentration Dispersions of Exfoliated MoS_2 with Increased Flake Size. *Chem. Mater.* **2012**, *24* (12), 2414–2421. https://doi.org/10.1021/cm301515z.

(18) Coleman, J. N. Liquid Exfoliation of Defect-Free Graphene. *Acc. Chem. Res.* **2013**, *46* (1), 14–22. https://doi.org/10.1021/ar300009f.

(19) Coleman, J. N.; Lotya, M.; O'Neill, A.; Bergin, S. D.; King, P. J.; Khan, U.; Young, K.; Gaucher, A.; De, S.; Smith, R. J.; Shvets, I. V.; Arora, S. K.; Stanton, G.; Kim, H.-Y.; Lee, K.; Kim, G. T.; Duesberg, G. S.; Hallam, T.; Boland, J. J.; Wang, J. J.; Donegan, J. F.; Grunlan, J. C.; Moriarty, G.; Shmeliov, A.; Nicholls, R. J.; Perkins, J. M.; Grieveson, E. M.; Theuwissen, K.; McComb, D. W.; Nellist, P. D.; Nicolosi, V. Two-Dimensional Nanosheets Produced by Liquid Exfoliation of Layered Materials. *Science* **2011**, *331* (6017), 568–571. https://doi.org/10.1126/science.1194975.

(20) Ogilvie, S. P.; Large, M. J.; O'Mara, M. A.; Lynch, P. J.; Lee, C. L.; King, A. A. K.; Backes, C.; Dalton, A. B. Size Selection of Liquid-Exfoliated 2D Nanosheets. *2D Mater.* **2019**, *6* (3), 031002. https://doi.org/10.1088/2053-1583/ab0dc3.

(21) Nagyte, V.; Kelly, D. J.; Felten, A.; Picardi, G.; Shin, Y.; Alieva, A.; Worsley, R. E.; Parvez, K.; Dehm, S.; Krupke, R.; Haigh, S. J.; Oikonomou, A.; Pollard, A. J.; Casiraghi, C. Raman Fingerprints of Graphene Produced by Anodic Electrochemical Exfoliation. *Nano Lett.* **2020**. https://doi.org/10.1021/acs.nanolett.0c00332.

(22) Silva, D. L.; Campos, J. L. E.; Fernandes, T. F. D.; Rocha, J. N.; Machado, L. R. P.; Soares, E. M.; Miquita, D. R.; Miranda, H.; Rabelo, C.; Vilela Neto, O. P.; Jorio, A.; Cançado, L. G. Raman Spectroscopy Analysis of Number of Layers in Mass-Produced Graphene Flakes. *Carbon* **2020**, *161*, 181–189. https://doi.org/10.1016/j.carbon.2020.01.050.

(23) Large, M. J.; Ogilvie, S. P.; Amorim Graf, A.; Lynch, P. J.; O'Mara, M. A.; Waters, T.; Jurewicz, I.; Salvage, J. P.; Dalton, A. B. Large-Scale Surfactant Exfoliation of

Graphene and Conductivity-Optimised Graphite Enabling Wireless Connectivity. *Adv. Mater. Technol.* **2020**. https://doi.org/10.1002/admt.202000284.

(24) Kim, Y.; Lee, E. J.; Roy, S.; Sharbirin, A. S.; Ranz, L.-G.; Dieing, T.; Kim, J. Measurement of Lateral and Axial Resolution of Confocal Raman Microscope Using Dispersed Carbon Nanotubes and Suspended Graphene. *Curr. Appl. Phys.* **2020**, *20* (1), 71–77. https://doi.org/10.1016/j.cap.2019.10.012.

(25) Backes, C.; Smith, R. J.; McEvoy, N.; Berner, N. C.; McCloskey, D.; Nerl, H. C.; O'Neill, A.; King, P. J.; Higgins, T.; Hanlon, D.; Scheuschner, N.; Maultzsch, J.; Houben, L.; Duesberg, G. S.; Donegan, J. F.; Nicolosi, V.; Coleman, J. N. Edge and Confinement Effects Allow in Situ Measurement of Size and Thickness of Liquid-Exfoliated Nanosheets. *Nat. Commun.* **2014**, *5* (1), 4576. https://doi.org/10.1038/ncomms5576.

(26) Malard, L. M.; Pimenta, M. A.; Dresselhaus, G.; Dresselhaus, M. S. Raman Spectroscopy in Graphene. *Phys. Rep.* **2009**, *473* (5–6), 51–87. https://doi.org/10.1016/j.physrep.2009.02.003.

(27) Ferrari, A. C.; Basko, D. M. Raman Spectroscopy as a Versatile Tool for Studying the Properties of Graphene. *Nat. Nanotechnol.* **2013**, *8* (4), 235–246. https://doi.org/10.1038/nnano.2013.46.

(28) Ferrari, A. C.; Meyer, J. C.; Scardaci, V.; Casiraghi, C.; Lazzeri, M.; Mauri, F.; Piscanec, S.; Jiang, D.; Novoselov, K. S.; Roth, S.; Geim, A. K. Raman Spectrum of Graphene and Graphene Layers. *Phys. Rev. Lett.* **2006**, *97* (18). https://doi.org/10.1103/PhysRevLett.97.187401.

(29) Backes, C.; Paton, K. R.; Hanlon, D.; Yuan, S.; Katsnelson, M. I.; Houston, J.; Smith, R. J.; McCloskey, D.; Donegan, J. F.; Coleman, J. N. Spectroscopic Metrics Allow in Situ Measurement of Mean Size and Thickness of Liquid-Exfoliated Few-Layer Graphene Nanosheets. *Nanoscale* **2016**, *8* (7), 4311–4323. https://doi.org/10.1039/C5NR08047A.

(30) Wieting, T. J.; Verble, J. L. Infrared and Raman Studies of Long-Wavelength Optical Phonons in Hexagonal Mo S 2. *Phys. Rev. B* **1971**, *3* (12), 4286–4292. https://doi.org/10.1103/PhysRevB.3.4286.

(31) Windom, B. C.; Sawyer, W. G.; Hahn, D. W. A Raman Spectroscopic Study of MoS2 and MoO3: Applications to Tribological Systems. *Tribol. Lett.* **2011**, *42* (3), 301–310. https://doi.org/10.1007/s11249-011-9774-x.

(32) Lee, J.-U.; Park, J.; Son, Y.-W.; Cheong, H. Anomalous Excitonic Resonance Raman Effects in Few-Layered MoS_2. *Nanoscale* **2015**, *7* (7), 3229–3236. https://doi.org/10.1039/C4NR05785F.

(33) Mignuzzi, S.; Pollard, A. J.; Bonini, N.; Brennan, B.; Gilmore, I. S.; Pimenta, M. A.; Richards, D.; Roy, D. Effect of Disorder on Raman Scattering of Single-Layer Mo S 2. *Phys. Rev. B* **2015**, *91* (19), 1954111–1954117. https://doi.org/10.1103/PhysRevB.91.195411.

(34) Rice, C.; Young, R. J.; Zan, R.; Bangert, U.; Wolverson, D.; Georgiou, T.; Jalil, R.; Novoselov, K. S. Raman-Scattering Measurements and First-Principles Calculations of Strain-Induced Phonon Shifts in Monolayer MoS 2. *Phys. Rev. B* **2013**, *87* (8). https://doi.org/10.1103/PhysRevB.87.081307.

(35) Chakraborty, B.; Bera, A.; Muthu, D. V. S.; Bhowmick, S.; Waghmare, U. V.; Sood, A. K. Symmetry-Dependent Phonon Renormalization in Monolayer MoS 2 Transistor. *Phys. Rev. B* **2012**, *85* (16). https://doi.org/10.1103/PhysRevB.85.161403.

(36) Verble, J. L.; Wieting, T. J. Lattice Mode Degeneracy in Mo S 2 and Other Layer Compounds. *Phys. Rev. Lett.* **1970**, *25* (6), 362–365. https://doi.org/10.1103/PhysRevLett.25.362.

(37) Frey, G. L.; Tenne, R.; Matthews, M. J.; Dresselhaus, M. S.; Dresselhaus, G. Raman and Resonance Raman Investigation of MoS 2 Nanoparticles. *Phys. Rev. B* **1999**, *60* (4), 2883–2892. https://doi.org/10.1103/PhysRevB.60.2883.

(38) Pimenta, M. A.; del Corro, E.; Carvalho, B. R.; Fantini, C.; Malard, L. M. Comparative Study of Raman Spectroscopy in Graphene and MoS_2 -Type Transition Metal

Dichalcogenides. *Acc. Chem. Res.* **2015**, *48* (1), 41–47. https://doi.org/10.1021/ar500280m.

(39) Fan, J.-H.; Gao, P.; Zhang, A.-M.; Zhu, B.-R.; Zeng, H.-L.; Cui, X.-D.; He, R.; Zhang, Q.-M. Resonance Raman Scattering in Bulk 2H-MX_2 (M = Mo, W; X = S, Se) and Monolayer MoS_2. *J. Appl. Phys.* **2014**, *115* (5), 053527. https://doi.org/10.1063/1.4862859.

(40) Gołasa, K.; Grzeszczyk, M.; Bożek, R.; Leszczyński, P.; Wysmołek, A.; Potemski, M.; Babiński, A. Resonant Raman Scattering in MoS 2 —From Bulk to Monolayer. *Solid State Commun.* **2014**, *197*, 53–56. https://doi.org/10.1016/j.ssc.2014.08.009.

(41) Chakraborty, B.; Matte, H. S. S. R.; Sood, A. K.; Rao, C. N. R. Layer-Dependent Resonant Raman Scattering of a Few Layer MoS_2: Raman Scattering of a Few Layer MoS_2. *J. Raman Spectrosc.* **2013**, *44* (1), 92–96. https://doi.org/10.1002/jrs.4147.

(42) Carvalho, B. R.; Wang, Y.; Mignuzzi, S.; Roy, D.; Terrones, M.; Fantini, C.; Crespi, V. H.; Malard, L. M.; Pimenta, M. A. Intervalley Scattering by Acoustic Phonons in Two-Dimensional MoS2 Revealed by Double-Resonance Raman Spectroscopy. *Nat. Commun.* **2017**, *8* (1). https://doi.org/10.1038/ncomms14670.

(43) Backes, C.; Szydłowska, B. M.; Harvey, A.; Yuan, S.; Vega-Mayoral, V.; Davies, B. R.; Zhao, P.; Hanlon, D.; Santos, E. J. G.; Katsnelson, M. I.; Blau, W. J.; Gadermaier, C.; Coleman, J. N. Production of Highly Monolayer Enriched Dispersions of Liquid-Exfoliated Nanosheets by Liquid Cascade Centrifugation. *ACS Nano* **2016**, *10* (1), 1589–1601. https://doi.org/10.1021/acsnano.5b07228.

(44) Huang, T.-X.; Cong, X.; Wu, S.-S.; Lin, K.-Q.; Yao, X.; He, Y.-H.; Wu, J.-B.; Bao, Y.-F.; Huang, S.-C.; Wang, X.; Tan, P.-H.; Ren, B. Probing the Edge-Related Properties of Atomically Thin MoS2 at Nanoscale. *Nat. Commun.* **2019**, *10* (1). https://doi.org/10.1038/s41467-019-13486-7.

(45) Kitajima, M. Defects in Crystals Studied by Raman Scattering. *Crit. Rev. Solid State Mater. Sci.* **1997**, *22* (4), 275–349. https://doi.org/10.1080/10408439708241263.

(46) Mignuzzi, S.; Pollard, A. J.; Bonini, N.; Brennan, B.; Gilmore, I. S.; Pimenta, M. A.; Richards, D.; Roy, D. Effect of Disorder on Raman Scattering of Single-Layer MoS2. *Phys. Rev. B* **2015**, *91* (19), 195411. https://doi.org/10.1103/PhysRevB.91.195411.

(47) Vancsó, P.; Magda, G. Z.; Pető, J.; Noh, J.-Y.; Kim, Y.-S.; Hwang, C.; Biró, L. P.; Tapasztó, L. The Intrinsic Defect Structure of Exfoliated MoS 2 Single Layers Revealed by Scanning Tunneling Microscopy. *Sci. Rep.* **2016**, *6* (1), 1–7. https://doi.org/10.1038/srep29726.

For Table of Contents Only